frontiers | Frontiers in Physics

TYPE Original Research
PUBLISHED 03 October 2025
DOI 10.3389/fphy.2025.1666941

OPEN ACCESS

EDITED BY
Chris Armstrong,
Science and Technology Facilities Council, United Kingdom

REVIEWED BY
Jose A. Pérez-Hernández,
Centro de Láseres Pulsados, Spain
Bhooshan Paradkar,
UM-DAE Centre for Excellence in Basic Sciences, India

*CORRESPONDENCE
Natsumi Iwata,
iwata.natsumi.ile@osaka-u.ac.jp

RECEIVED 16 July 2025
ACCEPTED 29 August 2025
PUBLISHED 03 October 2025

CITATION
Iwata N and Sentoku Y (2025) Energy partition of fast ions and fast electrons in foil plasma expansion under continuous irradiation with kJ petawatt laser light.
Front. Phys. 13:1666941.
doi: 10.3389/fphy.2025.1666941

Energy partition of fast ions and fast electrons in foil plasma expansion under continuous irradiation with kJ petawatt laser light

Natsumi Iwata* and Yasuhiko Sentoku

Institute of Laser Engineering, The University of Osaka, Osaka, Japan

Kilojoule-class relativistic-intensity lasers with multi-picosecond (ps) pulse durations can efficiently produce fast ions in interactions with thin foil plasmas via target normal sheath acceleration (TNSA). We derive the energy partition between fast ions and fast electrons during the expansion of a thin foil plasma irradiated by a relativistic-intensity laser over picosecond timescales. As the expansion proceeds with continuous laser heating, both ion and electron energies increase simultaneously. In this study, we show that the energy partition between fast electrons and fast ions converges to a steady-state level on a ps timescale. This level is determined by the time dependence of the effective temperature of fast electrons and the dimensionality of momentum space. The steady-state level is verified by particle-in-cell simulations. The theory can be used to predict the energy conversion efficiency from the laser to fast ions for applications such as laser-driven proton sources.

KEYWORDS

ion acceleration, kJ petawatt laser, high-intensity laser plasma interaction, plasma expansion, particle-in-cell simulation

1 Introduction

Laser-driven ion acceleration has gained a lot of interest as an application of high-power lasers with relativistic intensities over 10^{18} W/cm^2 [1, 2]. Recently, kilojoule (kJ)-class petawatt lasers have become available worldwide [3–6], opening a distinguished regime of ion acceleration with high efficiency. Experiments using the kJ-class lasers and thin foil targets demonstrate proton maximum energies of 10 MeV–50 MeV at intensity levels of 10^{18-19} W/cm^2, and the energy conversion rate from laser to fast protons with energies above several MeV [7–11] via target normal sheath acceleration (TNSA) is observed to be approximately 5% [1]. Such high-energy and high-flux ion beams can be used in applications such as radiography of dense plasmas [12, 13], neutron generation [14, 15], and fast ignition-based laser fusion [16, 17].

Modeling the energy conversion rate from laser to fast ions in the kJ laser-driven TNSA is important for the applications. In relativistic laser–foil interactions, electrons at the laser-irradiated front surface of the foil are accelerated by the laser field and launched into the overdense foil plasma. The laser-accelerated fast electrons create an

electric field surrounding the foil, which accelerates ions, leading to a quasi-neutral plasma expansion. Hence, in TNSA, the laser energy is initially converted predominantly into fast electrons, after which a portion of the electron energy is transferred to fast ions during the expansion. The quasi-neutral plasma expansion proceeds with the timescale of ion fluid motion characterized by $2\pi\omega_{pi}^{-1}$, where $\omega_{pi} = (4\pi n_i Z^2 e^2/M_i)^{1/2}$ is the ion plasma frequency, n_i is the ion density, Z is the ion charge state, e is the elementary charge, and M_i is the ion mass. The timescale $2\pi\omega_{pi}^{-1}$ at the critical density $n_c = m_e\omega_L^2/(4\pi e^2)$ is in the order of 100 femtoseconds (fs) for the laser wavelength of $\lambda_L = 1$ μm, where ω_L is the laser frequency and m_e is the rest mass of an electron. Therefore, when a laser pulse with relativistic intensity and a multi-picosecond (ps) pulse duration irradiates a foil target, as in the case of kJ petawatt lasers, electron heating by the laser and ion energy gain through plasma expansion occur simultaneously, which is different from the adiabatic expansion [18–20].

When the laser pulse duration is sub-ps or shorter, the effective temperature of fast electrons T_e remains near the ponderomotive temperature $T_p = (\gamma_e - 1)m_e c^2$, where $\gamma_e = (1 + a_0^2/2)^{1/2}$ is the average relativistic factor of fast electrons determined by the electron oscillation energy in the linearly polarized laser electric field with the normalized amplitude $a_0 = eE_L/m_e c\omega_L$ (where E_L is the laser electric field and c is the speed of light) [21]. On the other hand, when the pulse duration is over-ps, T_e increases temporally beyond T_p during the interaction [22–25], while the plasma expands on a similar timescale. This indicates that a portion of the laser energy is used to heat fast electrons, while the remainder is converted into the kinetic energy of fast ions.

In this paper, we derive the temporal evolution of energies of fast electrons and ions in the expanding plasma under relativistic-intensity laser irradiation based on the non-isothermal plasma expansion model [26], which takes into account the temporal evolution of the effective fast electron temperature during the interaction. The energy partition between fast ions and fast electrons converges to a steady-state level on a ps timescale. The level is determined by the time-dependence of the effective fast electron temperature and the dimensionality of the momentum distribution of fast electrons. The theory derived in Section 2 is verified by one-dimensional (1D) and two-dimensional (2D) particle-in-cell (PIC) simulations in Section 3. Section 4 presents a discussion on the energy conversion efficiency in proton acceleration and provides the conclusion.

2 Theory

We consider the quasi-neutral expansion of a thin foil plasma irradiated by a laser light with a relativistic amplitude $a_0 > 1$. The expanding plasma is composed of ions and fast electrons with an effective temperature T_e, following a Boltzmann distribution. In this study, we refer to the ions in the expanding plasma as 'fast ions' to distinguish them from the bulk ions in the foil. We model the plasma expansion in 1D geometry since the kJ lasers have large spot sizes that are typically over 50 μm, and the expansion can be treated as 1D up to several ps without lateral energy loss [27]. We limit the discussion here to a non-relativistic regime for ions, where the ion sound velocity $C_s = (ZT_e/M_i)^{1/2}$ is much slower than c and the ions are cold, $T_i \simeq 0$.

We define the areal energy density of ions in the expanding plasma in the rear side of the foil as follows:

$$U_i(t) \equiv \int_{-R}^{x_f} \frac{1}{2} M_i v_i^2(x,t)\, n_i(x,t)\, dx. \tag{1}$$

We define that of fast electrons as follows:

$$U_e(t) \equiv \int_{-R}^{x_f} \frac{N}{2} T_e(t)\, n_e(x,t)\, dx, \tag{2}$$

where N is the degree of freedom of fast electrons in momentum space, v_i is the ion fluid velocity, and $n_e = n_i/Z$ is the electron density. Here, the plasma occupies the area of $x \le 0$ initially with an ion density n_{i0} and expands from $x = -R$ to the front position $x_f(t)$, where the quasi-neutral condition is satisfied for $x < x_f$. Here,

$$R(t) = \int_0^t C_s(t')\, dt', \tag{3}$$

which is the scale length of the expansion at time t. U_i, obtained using Equation 1, is the ion kinetic energy associated with the expansion per unit area, and U_e, obtained using Equation 2, corresponds to the internal energy owned by fast electrons with an effective temperature T_e per unit area.

Here, we use n_i and v_i derived using the non-isothermal plasma expansion model [26].

$$n_i(x,t) = n_{i0} \exp\left[-\left(1 + \frac{x}{R}\right) + \frac{\varepsilon}{2}\left(2 - \frac{x}{R}\right)\right], \tag{4}$$

$$v_i(x,t) = C_s\left(1 + \frac{x}{R} - \frac{\varepsilon}{2}\frac{x}{R}\right), \tag{5}$$

which takes into account the time evolution of T_e up to the first order of the smallness parameter εdefined as

$$\varepsilon(t) \equiv \frac{R\dot{C}_s}{C_s^2}. \tag{6}$$

$\varepsilon < 1$ indicates that the timescale of the temperature evolution, $(d(\log T_e)/dt)^{-1} = (2\dot{C}_s/C_s)^{-1}$, is slower than that of the plasma expansion R/C_s, where the dot denotes the time derivative and R is given by Equation 3. For $\varepsilon = 0$, Equations 4, 5 reproduce the self-similar solution for the isothermal plasma expansion [28, 29]. The model is applicable for the timescale $\omega_{pi}t \gg 1$.

Substituting Equations 4, 5 into Equations 1, 2 and using the relation $C_s^2 = n_{e0}T_e/(n_{i0}M_i)$, we obtain the following:

$$U_i(t) = \frac{n_{i0}M_i C_s^2 R}{1 + \varepsilon/2} \exp\left(\frac{3\varepsilon}{2}\right) \times \left(A_1 - A_2 \exp\left[-\left(\frac{x_f}{R} + 1\right)\left(1 + \frac{\varepsilon}{2}\right)\right]\right), \tag{7}$$

$$U_e(t) = \frac{N}{2}\frac{n_{i0}M_i C_s^2 R}{1 + \varepsilon/2} \exp\left(\frac{3\varepsilon}{2}\right) \times \left(1 - \exp\left[-\left(\frac{x_f}{R} + 1\right)\left(1 + \frac{\varepsilon}{2}\right)\right]\right), \tag{8}$$

where the coefficients A_1 and A_2 are given by the following Equations 9, 10.

$$A_1 = \frac{1 - \varepsilon}{(1 + \varepsilon/2)^2} + \frac{\varepsilon}{2 + \varepsilon}, \tag{9}$$

$$A_2 = \frac{\left(1 + x_f/R\right)^2(1 - \varepsilon)}{2} + \frac{1 + x_f/R}{2}\left(\frac{2(1 - \varepsilon)}{1 + \varepsilon/2} + \varepsilon\right) + A_1, \tag{10}$$

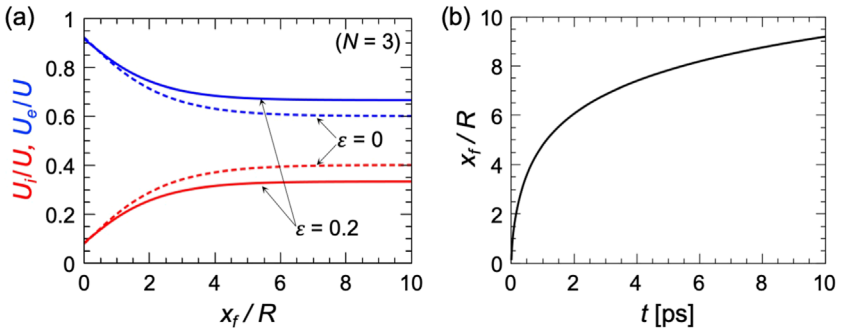

FIGURE 1
(a) Energy partitions of fast electrons U_e/U (blue) and fast ions U_i/U (red) for $N = 3$ as a function of x_f/R. Dashed lines are Equations 8, 7 with $\varepsilon = 0$, and solid lines are those with $\varepsilon = 0.2$. **(b)** Dependence of x_f/R on the time given by Equation 11, where ω_{pi0} is evaluated for deuteron ions at the critical density for an electromagnetic wavelength of 1 μm.

and the terms of order ε^n ($n \geq 2$) are neglected. The time dependence is included in the scale length R, the smallness parameter ε, and the front position x_f, which is given by

$$x_f(t) \simeq \frac{R}{\tau}\left[\tau \ln\left(\tau + \sqrt{\tau^2+1}\right) - \sqrt{\tau^2+1} + 1\right], \tag{11}$$

with an approximation $R \simeq C_s t$ as the isothermal model [29], where $\tau = \omega_{pi0} t/\sqrt{2\exp(1)}$ and ω_{pi0} is the ion plasma frequency at $n_i = n_{i0}$.

We plot Equations 7, 8 for $N = 3$ normalized by the total areal energy density $U \equiv U_i + U_e$ in Figure 1a as a function of x_f/R, which is the front position normalized by the expansion scale length.

The dashed and solid lines are represent $\varepsilon = 0$ and $\varepsilon = 0.2$, respectively. Note that $\varepsilon = 0$ is the case where the effective electron temperature T_e is constant temporally, and $\varepsilon = 0.2$ denotes that T_e increases gradually during the expansion. The temporal evolution of x_f/R given by Equation 11 is shown in Figure 1b, where ω_{pi0} is evaluated for deuteron ions at the critical density $n_{i0} = n_c$ for the laser wavelength $\lambda_L = 1$ μm, i.e., $2\pi\omega_{pi0}^{-1} \approx 200$ fs. In the early stage, where $x_f/R \gg 1$ is not satisfied, fast electrons carry the dominant share of the energy. The ion energy partition increases afterward, and in the later stage $x_f/R \gtrsim 5$, the energy partition converges to a steady-state level, i.e., $U_i/U = 0.4$ for $\varepsilon = 0$. Note that Equation 11 is valid under the approximation $R \simeq C_s t$, and therefore, Figure 1b has an accuracy of the zeroth order of ε. The steady-state level of the energy partition is derived under the long time approximation $x_f/R \gg 1$, by which Equations 7, 8 are reduced to the following:

$$U_i(t) = \frac{n_{i0} M_i C_s^2 R}{1+\varepsilon/2} A_1 \exp\left(\frac{3\varepsilon}{2}\right), \tag{12}$$

$$U_e(t) = \frac{n_{i0} M_i C_s^2 R}{1+\varepsilon/2} \frac{N}{2} \exp\left(\frac{3\varepsilon}{2}\right). \tag{13}$$

The energy partitions U_i/U and U_e/U are then obtained from Equations 12, 13 as follows:

$$\frac{U_i}{U} = \frac{2}{2+N}\left(1 - \frac{3\varepsilon}{2}\frac{N}{2+N}\right), \tag{14}$$

$$\frac{U_e}{U} = \frac{N}{2+N}\left(1 + \frac{3\varepsilon}{2}\frac{2}{2+N}\right), \tag{15}$$

in the first order of ε. When the time evolution of ε is negligible, Equations 14, 15 are time-independent, which denotes that the energy partition reaches to a quasi-steady-state on the long timescale $x_f/R \gg 1$. The steady-state levels of Equations 14, 15 are determined by the temporal evolution of the fast electron effective temperature represented by ε and the dimensionality of the momentum distribution of fast electrons N. The values of U_i/U and U_e/U for $\varepsilon = 0$ are shown in Table 1.

The energy partition of fast ions decreases as N increases because the momentum coupling from fast electrons to the 1D ion expansion becomes weaker. In the laser–foil interaction, the plasma expansion that takes place both at the front and rear sides of the foil is nearly symmetrical [11, 30, 31] due to the recirculation of fast electrons in the expanding plasma. Therefore, the total areal energy densities of fast ions and fast electrons in the foil expansion on both sides are expected to be twice those given by Equations 12, 13, while their ratios, Equations 14, 15, remain valid for the expansion on both sides.

After the laser irradiation ends, the plasma expansion becomes adiabatic. In the ideal case where the interaction after the laser irradiation is 1D without energy dissipation, the ion energy partition increases while satisfying the energy conservation $d(U_e + U_i + U_{field})/dt = 0$ [19, 20], where U_{field} is the areal energy density of the field. In this case, $U_i/U \simeq 1$ can be achieved eventually after electron cooling by the expansion. In multidimensional situations, the lateral energy loss limits U_i/U in the adiabatic expansion. The energy gain of fast ions will then be dominated by the acceleration during the laser energy input, especially for the case of multi-ps pulse lasers. In contrast, when the laser pulse duration is shorter than $2\pi\omega_{pi}^{-1}$, which is approximately 200 fs for $n_i = n_c$ for deuterium plasmas, the adiabatic process after the pulse time plays an important role in determining the ion energy gain. Therefore, the energy partitions given by Equations 14, 15 are applicable to describe TNSA by the kJ lasers that have pulse durations much longer than $2\pi\omega_{pi}^{-1}$ and spot sizes that are sufficiently larger than the expansion length.

As shown in Figure 1a, the energy partitions converge to the values described by Equations 14, 15 when $x_f/R \gtrsim 5$. The time t for this condition is estimated on the zeroth order of ε from Equation 11 as follows:

$$\omega_{pi0} t \geq \exp\left(4 - \ln\sqrt{2}\right) \approx 39, \tag{16}$$

TABLE 1 Ratio of the ion energy U_i and electron energy U_e given by Equations 14, 15 for $\varepsilon = 0$.

Electron momentum dimension N	Ion energy partition U_i/U (ε=0)	Electron energy partition U_e/U (ε=0)
1	2/3	1/3
2	1/2	1/2
3	2/5	3/5

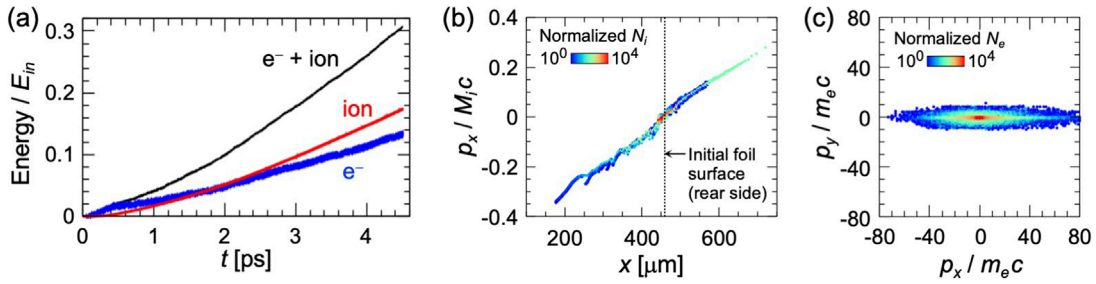

FIGURE 2
One-dimensional PIC simulation result. **(a)** Temporal evolution of energies of electrons (blue) and ions (red). The black line is the sum of the electron and ion energies. The values are normalized by the total input laser energy E_{in} up to the final time of the simulation, $t = 4.5$ ps. **(b)** Ion distribution in the phase space x–p_x at $t = 4.5$ ps. The initial foil surface position at the rear side is indicated by the dotted line. **(c)** Electron distribution in momentum space p_x–p_y at $t = 4.5$ ps.

where we used the approximation $\omega_{pi0}t \gg 1$ in Equation 11. For ω_{pi0} of deuteron ions at the critical density for the laser wavelength λ_L = 1 μm, Equation 16 yields $t \gtrsim 1.2$ ps. Hence, one can expect that the steady-state energy levels given by Equations 12, 13 are achieved on a ps timescale.

3 PIC simulation

We verify the above theoretical model by 1D and 2D PIC simulations using the PICLS code [32]. In the simulations, a foil plasma is irradiated by a laser from the left side with a wavelength of 1 μm and p-polarization. The foil is modeled as a fully ionized deuterium (D) plasma, and the initial electron and ion temperatures are 0. The laser amplitude a_0 increases exponentially with a Gaussian profile of temporal width $\tau_{\rm rise}$ to the peak amplitude $\hat{a}_0$, and it stays constant afterward.

To examine the expansion with $N = 1$, i.e., a 1D electron momentum distribution, we use a 1D PIC simulation that does not include Coulomb collisions. The foil thickness is 5 μm, and the initial density of the foil is $233\,n_c$. We place a pre-plasma having an exponential profile with a scale length of 5 μm. The foil surface is located initially at $x = 453$ μm in the 1000 μm-long simulation box. $t = 0$ is the time at which the laser front reaches the foil surface position. The laser peak amplitude is $\hat{a}_0 = 2$, and the rise time is $\tau_{\rm rise} = 70$ fs. The mesh size is 0.017 μm, and 15 particles per cell are used for each species.

The temporal evolution of energy in the 1D simulation system is shown in Figure 2a. The values are normalized by the total input laser energy E_{in} up to the final time of the simulation, $t = 4.5$ ps. The electron energy increases rapidly at early time $t < 0.5$ ps, and the ion energy catches up to the electron energy on a ps timescale by the plasma expansion. The ion expansion front at the rear-side at the final time $t = 4.5$ ps is approximately 200 μm away from the initial target position, as shown in (b), which presents the ion distribution in the x–p_x plane.

In (b), the maximum absolute value of p_x at the front side is approximately 1.2 times larger than that at the rear side, while the ratio of the total energy of ions at the front side $x < 453$ μm, E_f, and that at the rear side $x > 458$ μm, E_r, was E_f:E_r = 0.39:0.61. The expansion is, thus, not completely symmetric, which can cause a deviation of the simulation results from the theoretical prediction. Figure 2c shows the electron distribution in the momentum space p_x–p_y. The distribution is almost 1D, $p_y \ll p_x$, and therefore, $N = 1$ is applicable for this interaction.

The slope temperature of fast electrons increases temporally, as observed from the electron energy distributions in Figure 3a, where the distributions are composed of all the electrons in the simulation system. In Figure 3b, the slope temperatures T_e obtained by the fitting of the electron energy distribution is shown by crosses, where the Maxwell distribution proportional to $\exp(-E_e/T_e)$ is assumed for the fitting. Here, E_e is the electron energy, and the fitting lines are shown by the black dashed lines in (a). Circles filled with blue in (b) are the average energy E_{av} of electrons whose energies are above 0.2 MeV, which is approximately half of the ponderomotive energy. The value of E_{av} is approximately half of the slope temperature T_e at the same time, which indicates that the relation $E_{av} = T_e N/2$ with $N = 1$, i.e., the 1D momentum distribution of the fast electrons, is satisfied in this interaction. Here, we fit E_{av} with $E_{av} = T_0(1 + (t/\tau)^\alpha)N/2$ for $N = 1$ and $\alpha = 1$, as

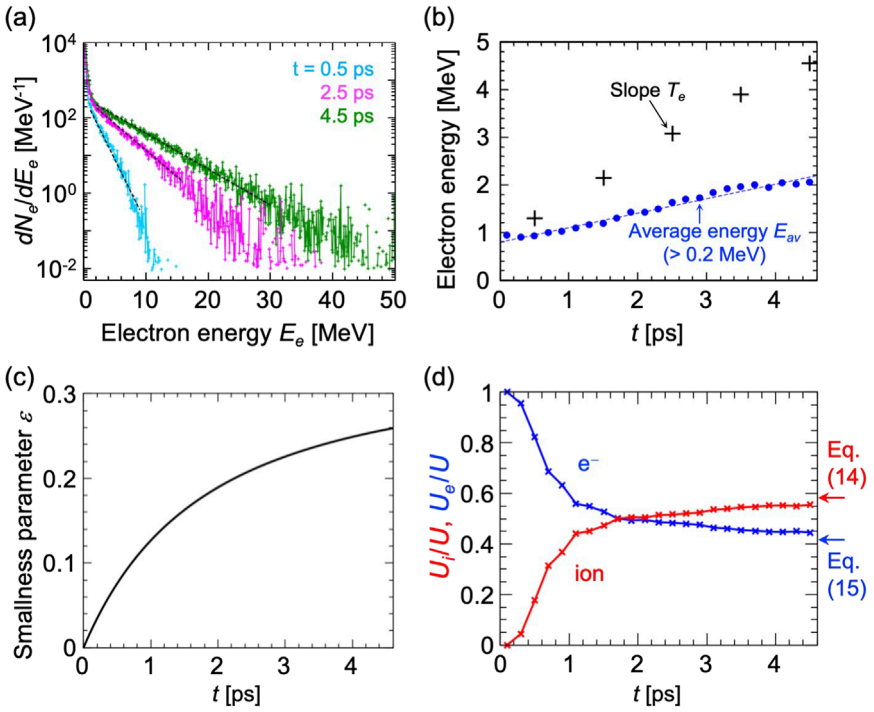

FIGURE 3
(a) Temporal evolution of the electron energy distribution in the 1D PIC simulation. The vertical axis is in logarithmic scale. **(b)** Temporal evolution of the average energy E_{av} of electrons whose energies are above 0.2 MeV (filled circles), and the slope temperature T_e of fast electrons (crosses). T_e is obtained by the fitting of the energy distributions as the black dotted lines in **(a)** with Maxwell distributions proportional to $\exp(-E_e/T_e)$. The dotted line in **(b)** is a fitting line of the average energy E_{av} using $E_{av} = T_0(1+(t/\tau)^\alpha)N/2$ for $N = 1$ and $\alpha = 1$, which results in $T_0 = 1.6$ MeV and $\tau = 2.7$ ps. **(c)** Temporal evolution of the smallness parameter ε obtained from the fitting line in **(b)**. **(d)** Temporal evolution of the energy partition of fast ions U_i/U and fast electrons U_e/U. The arrows on the right side of panel **(d)** indicate the values of U_i/U and U_e/U calculated from Equations 14, 15 for $N = 1$ and ε at the final time of the simulation $t = 4.5$ ps in **(c)**.

shown by the blue dashed line in (b). This fit yields the parameter values $T_0 = 1.6$ MeV and $\tau = 2.7$ ps. The temporal evolution of T_e is then obtained from the relation $T_e = 2E_{av}/N$, and the smallness parameter ε defined by Equation 6 is calculated for $N = 1$ as shown in Figure 3c. As shown in Figure 3c, $\varepsilon < 0.3$ is maintained during the simulation, and therefore, the theory in Section 2 that assumes $\varepsilon \ll 1$ is applicable.

Figure 3d presents the temporal evolution of the energy partitions of the fast electrons and fast ions in the 1D simulation. For fast electrons, we calculated the sum of the energies of electrons whose energies are above 0.2 MeV. This corresponds to U_e defined by Equation 2 multiplied by the length of the simulation box in the y-direction. For fast ions, we calculated the sum of energy of ions whose energies are above 1 MeV as the corresponding value for U_i. The calculated values are then divided by the total particle energy, $U = U_e + U_i$, to show the energy partitions U_e/U and U_i/U. The fast ion energy partition increases and tends to saturate after approximately 1.5 ps. This timescale agrees with that indicated by Equation 16, i.e., $t \gtrsim 1.2$ ps for ω_{pi0} of deuteron ions at the critical density. Theoretical values of U_i/U and U_e/U under the long time approximation $x_f/R \gg 1$ in Equations 14, 15 are indicated by red and blue arrows, respectively. Here, we substitute $N = 1$, and $\varepsilon = 0.26$, which is obtained from Figure 3c at the final time of the simulation. The theory well-predicts the saturation values of the energy partition.

To investigate the energy partition with a multidimensional electron momentum distribution, we perform 2D PIC simulations. The 2D simulation includes Coulomb collisions, and a hydrogen plasma layer is attached to the backside of the deuterium foil to model a realistic TNSA by a kJ laser. The laser peak amplitude is $\hat{a}_0 = 1.6$, the spot radius is $r = 25$ μm, and the laser amplitude a_0 increases with a Gaussian profile, having a temporal width of 1.7 ps, to the peak amplitude $\hat{a}_0$ and remains constant afterward. The thicknesses of the deuterium foil and the hydrogen layer are 3.4 μm and 100 nm, respectively, and the plasma is distributed uniformly in the y-direction, initially with a density of $103\,n_c$ for the deuterium foil and $100\,n_c$ for the hydrogen layer. The initial position of the front surface of the foil is $x = 216$ μm. The laser front reaches the foil surface position at $t = 0$ with a normalized amplitude of $a_0 = 0.1$. The amplitude at the foil surface exceeds $a_0 = 1$ at $t = 1.02$ ps, assuming that the laser propagation speed is c. In front of the deuterium foil, pre-plasma is initially distributed at a scale length of 14 μm. The simulation box size is $(x, y) = (500\ \mu\text{m}, 198\ \mu\text{m})$, the mesh size is 0.025 μm, and the number of particles per cell per species is 15.

The energy of ions increases gradually with the plasma expansion after approximately 1.5 ps, as shown in Figure 4a, which shows the temporal evolution of particle energies in the simulation system normalized by the input laser energy E_{in}. Figure 4b presents the spatial distributions of the electric field in the x-direction E_x averaged over the laser cycle, i.e., the sheath

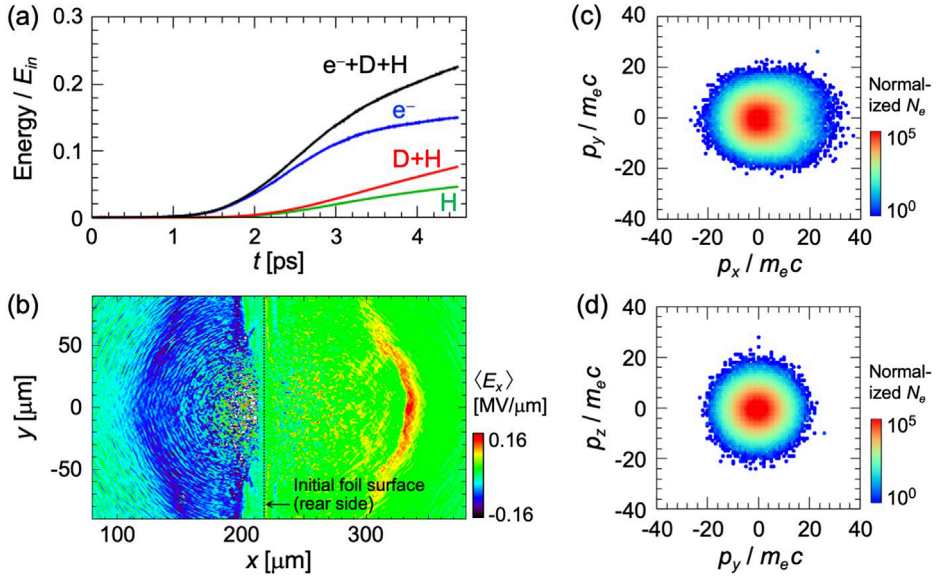

FIGURE 4
Two-dimensional PIC simulation result. **(a)** Temporal evolution of the energies of electrons (blue), protons (green), and all ions, including deuterium ions and protons (red). The black line is the sum of the electron and ion energies. The values are normalized by the total input laser energy E_{in} up to the final time of the simulation $t = 4.5$ ps. **(b)** Electric field in the x-direction E_x at $t = 4.3$ ps averaged over the laser period. The initial foil surface position at the rear side is indicated by the dotted line. Electron distribution in momentum space **(c)** p_x–p_y and **(d)** p_y–p_z at $t = 4.3$ ps. The color indicates the normalized number of electrons.

electric field, at $t = 4.3$ ps. The front position of the positive E_x field represents the plasma expansion front. The expansion front is approximately 110 μm away from the initial position of the backside surface of the foil, indicated by the black dotted line. As shown in Figures 4c, d, the electron momentum distribution is three-dimensional and nearly isotropic, differing from the 1D case shown in Figure 2c. Here, the momentum distributions are observed within the central area $|y| \le r/2$, where r is the laser spot radius.

From the electron energy distributions in $|y| \le r/2$ shown in Figure 5a, we obtained the average energy E_{av} and the slope temperature T_e of fast electrons in (b) using the same procedure as in the 1D PIC simulation. The ratio between T_e and E_{av} at the same time is 0.75 (average). Assuming the relation $T_e = 2E_{av}/N$, the effective degree of freedom in the electron momentum space is $N = 2.66$, which is between 3D ($N = 3$) and 2D ($N = 2$). This reflects the momentum distribution in Figures 4c,d, which is not perfectly isotropic. We fit E_{av} with $E_{av} = T_0(1 + ((t - t_0)/\tau)^{\alpha})N/2$ for $N = 3$, $\alpha = 1/2$, and $t_0 = 1$ ps, as shown by the blue dashed line in Figure 5b. This fit yields the parameter values $T_0 = 0.11$ MeV and $\tau = 0.045$ ps. Note that, at approximately $t = 1$ ps, the laser amplitude at the foil surface exceeds $a_0 = 1$ in this simulation. Figure 5c shows the smallness parameter ε of Equation 6 calculated for $N = 3$ using the fitting line in Figure 5b and the relation $T_e = 2E_{av}/N$. It is observed that $\varepsilon \ll 1$ is also satisfied in this 2D simulation. Compared with the 1D simulation, E_{av} and ε in Figures 5b, c increase rapidly just after $t = 1$ ps. This is attributed to the increase in energy absorption due to a multidimensional effect associated with the plasma surface modulation occurring on the timescale of the electron plasma frequency [33].

In Figure 5d, we show the temporal evolution of the energy partitions of fast electrons and fast ions in $|y| \le r/2$ in the 2D simulation, which are calculated using the same method as in the 1D simulation. The ion energy partition U_i/U (red) increases temporally and tends to saturate, as predicted by the theory, after approximately $t = 4$ ps. The saturation levels of U_i/U and U_e/U derived from Equations 14, 15 are indicated by the arrows on the right side of the panel (d), where we substitute $N = 3$ and $\varepsilon = 0.19$, which is the final value of ε in Figure 5c, into Equations 14, 15. The simulation and theoretical results are close, but the ion energy partition U_i/U in the simulation is approximately 20% lower than the theoretical value. The reduction is due to the multidimensionality of the plasma expansion, i.e., the expansion length becomes larger than the laser spot diameter, as shown in Figure 4b during the multi-ps interaction, and also due to errors in fitting the average energy of fast electrons in Figure 5b.

4 Discussion and conclusion

Equations 14, 15 can be used to predict the energy conversion efficiency η_i from laser to protons accelerated by TNSA at the rear side of the foil when the laser absorption rate from laser to plasma, η_{ab}, is known. We assume that the absorbed energy is converted to the particle energies in the expanding plasma at the front and rear sides of the foil equally. The energy conversion efficiency to fast ions at the rear side of the foil is then written as

$$\eta_i = \frac{\eta_{ab}}{2}\frac{U_i}{U}, \tag{17}$$

where U_i/U is given by Equation 14. In most cases, the rear-side plasma is occupied by protons from the contaminant layer,

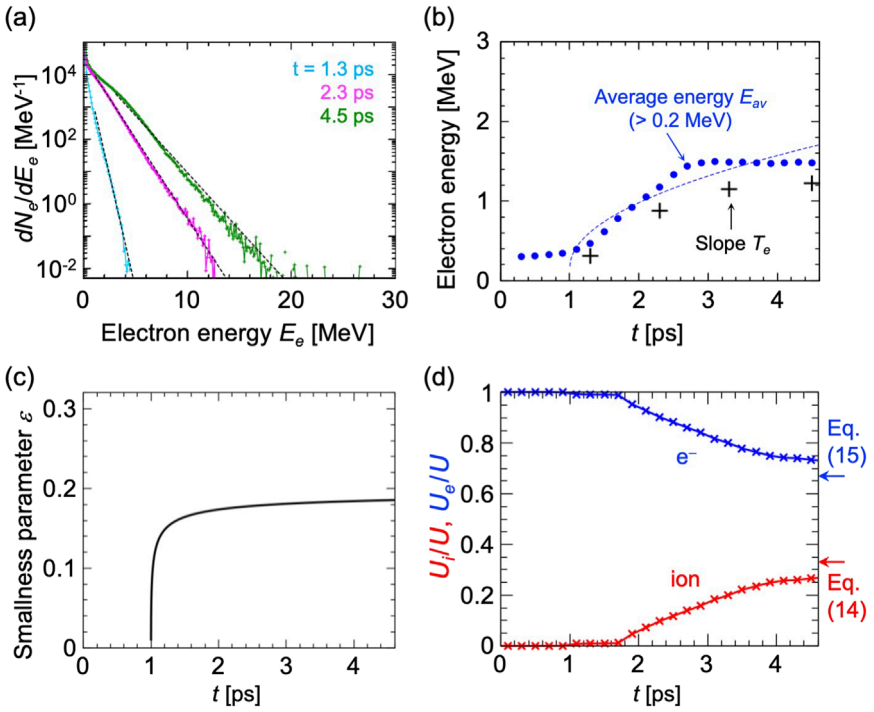

FIGURE 5
(a) Temporal evolution of the electron energy distribution in the 2D PIC simulation. The vertical axis is in logarithmic scale. **(b)** Temporal evolution of the average energy E_{av} of electrons whose energies are above 0.2 MeV (filled circles) and the slope temperature T_e of fast electrons (crosses). T_e is obtained by the fitting of the energy distributions as the black dotted lines in **(a)** with Maxwell distributions proportional to $\exp(-E_e/T_e)$. The dotted line in **(b)** is a fitting line of the average energy E_{av} using $E_{av} = T_e N/2$ and $T_e = T_0(1+((t-t_0)/\tau)^\alpha)$ for $N = 3$, $\alpha = 0.5$, and $t_0 = 1$ ps, which results in $T_0 = 0.11$ MeV and $\tau = 0.045$ ps. **(c)** Temporal evolution of the smallness parameter ε obtained from the fitting line in **(b)**. **(d)** Temporal evolution of the energy partition of fast ions U_i/U and fast electrons U_e/U. The arrows on the right side of the panel **(d)** indicate the values of U_i/U and U_e/U calculated from Equations 14, 15 for $N = 3$ and ε at the final time of the simulation $t = 4.5$ ps in **(c)**.

and thus, Equation 17 corresponds to the energy conversion efficiency from laser to protons. Equation 17 indicates that, for the multidimensional case $N = 3$, the absorbed energy is converted to the fast protons at a rate of $1/(2+N) = 1/5$ at the maximum by TNSA during the laser irradiation.

For the 2D simulation in Section 3, the black line in Figure 4a indicates $\eta_{ab} = 0.23$ at a final time $t = 4.5$ ps, and Equation 14 yields $U_i/U = 0.33$, as indicated by the red arrow in Figure 5d. Substituting them into Equation 17, we obtain $\eta_i = 3.8\,\%$. In the simulation, Figure 4a shows that the ratio of the total proton energy and the input energy, which is equivalent to η_i, is 4.6% at $t = 4.5$ ps (green line). Hence, the theoretical and simulation results are in close agreement, with a relative error of 17%. Although protons gain energy further in the adiabatic expansion after the pulse irradiation, the energy gain during the pulse irradiation dominantly determines the energy conversion efficiency to protons in the kJ laser interactions [34] because of the large-scale plasma expansion within the multi-ps pulse time.

In conclusion, we derived the energy partition of fast ions and fast electrons in a foil plasma expansion under kJ relativistic laser irradiation. The expansion proceeds with the over-picosecond laser heating, and energies of both fast ions and fast electrons increase simultaneously. Based on the non-isothermal quasi-neutral plasma expansion theory in 1D geometry, we find that the energy partition between fast ions and fast electrons converges to a steady-state level on a ps timescale. The level is determined by the time dependence of the effective temperature of fast electrons and their momentum distribution dimensionality. The theory is tested by PIC simulations in 1D and 2D geometry with a large laser spot ($r = 25\,\mu$m). In both cases, the energy partition converges to a steady-state level close to that predicted by the theory. The derived formula can be used to predict the energy conversion efficiency to fast ions in kJ laser experiments, which is important for applications of laser-driven ion sources, such as proton radiography and plasma heating in laser fusion.

Data availability statement

The original contributions presented in the study are included in the article/supplementary material; further inquiries can be directed to the corresponding author.

Author contributions

NI: Conceptualization, Writing – original draft, Formal analysis. YS: Conceptualization, Writing – review and editing.

Funding

The author(s) declare that financial support was received for the research and/or publication of this article. This study was supported by JSPS KAKENHI (grant numbers JP23K03354, JP24H00204, and JP23K20038) and JST PRESTO (grant no. JPMJPR21O1).

Acknowledgments

The authors are grateful to A. J. Kemp and S. C. Wilks for helpful discussions.

Conflict of interest

The authors declare that the research was conducted in the absence of any commercial or financial relationships that could be construed as a potential conflict of interest.

Generative AI statement

The author(s) declare that no Generative AI was used in the creation of this manuscript.

Any alternative text (alt text) provided alongside figures in this article has been generated by Frontiers with the support of artificial intelligence and reasonable efforts have been made to ensure accuracy, including review by the authors wherever possible. If you identify any issues, please contact us.

Publisher's note

References

1. Macchi A, Borghesi M, Passoni M. Ion acceleration by superintense laser-plasma interaction. *Rev Mod Phys* (2013) 85:751–93. doi:10.1103/RevModPhys.85.751

2. Daido H, Nishiuchi M, Pirozhkov AS. Review of laser-driven ion sources and their applications. *Rep Prog Phys* (2012) 75:056401. doi:10.1088/0034-4885/75/5/056401

3. Miyanaga N, Azechi H, Tanaka KA, Kanabe T, Jitsuno T, Kawanaka J, et al. 10-kj pw laser for the firex-i program. *J Phys IV France* (2006) 133:81–7. doi:10.1051/jp4:2006133016

4. Crane JK, Tietbohl G, Arnold P, Bliss ES, Boley C, Britten G, et al. Progress on converting a nif quad to eight, petawatt beams for advanced radiography. *J Phys Conf Ser* (2010) 244:032003. doi:10.1088/1742-6596/244/3/032003

5. Maywar DN, Kelly JH, Waxer LJ, Morse SFB, Begishev IA, Bromage J, et al. Omega ep high-energy petawatt laser: progress and prospects. *J Phys Conf Ser* (2008) 112:032007. doi:10.1088/1742-6596/112/3/032007

6. Miquel J-L, Prene E. LMJ and PETAL status and program overview. *Nucl Fusion* (2018) 59:032005. doi:10.1088/1741-4326/aac343

7. Yogo A, Mima K, Iwata N, Tosaki S, Morace A, Arikawa Y, et al. Boosting laser-ion acceleration with multi-picosecond pulses. *Scientific Rep* (2017) 7:42451. doi:10.1038/srep42451

8. Mariscal D, Ma T, Wilks SC, Kemp AJ, Williams GJ, Michel P, et al. First demonstration of arc-accelerated proton beams at the national ignition facility. *Phys Plasmas* (2019) 26:043110. doi:10.1063/1.5085787

9. Margarone D, Morace A, Bonvalet J, Abe Y, Kantarelou V, Raffestin D, et al. Generation of alpha-particle beams with a multi-kj, peta-watt class laser system. *Front Phys* (2020) 8:343. doi:10.3389/fphy.2020.00343

10. Raffestin D, Lecherbourg L, Lantuéjoul I, Vauzour B, Masson-Laborde PE, Davoine X, et al. Enhanced ion acceleration using the high-energy petawatt petal laser. *Matter Radiat Extremes* (2021) 6:056901. doi:10.1063/5.0046679

11. Campbell PT, Canning D, Hussein AE, Ratnayaka KDW, Thomas AGR, Krushelnick K, et al. Proton beam emittance growth in multipicosecond laser-solid interactions. *New J Phys* (2019) 21:103021. doi:10.1088/1367-2630/ab4721

12. Mackinnon AJ, Patel PK, Borghesi M, Clarke RC, Freeman RR, Habara H, et al. Proton radiography of a laser-driven implosion. *Phys Rev Lett* (2006) 97:045001. doi:10.1103/PhysRevLett.97.045001

13. Simpson RA, Mariscal DA, Kim J, Scott GG, Williams GJ, Grace E, et al. Demonstration of tnsa proton radiography on the national ignition facility advanced radiographic capability (nif-arc) laser. *Plasma Phys Controlled Fusion* (2021) 63:124006. doi:10.1088/1361-6587/ac2349

14. Yogo A, Lan Z, Arikawa Y, Abe Y, Mirfayzi SR, Wei T, et al. Laser-driven neutron generation realizing single-shot resonance spectroscopy. *Phys Rev X* (2023) 13:011011. doi:10.1103/PhysRevX.13.011011

15. Kleinschmidt A, Bagnoud V, Deppert O, Favalli A, Frydrych S, Hornung J, et al. Intense, directed neutron beams from a laser-driven neutron source at phelix. *Phys Plasmas* (2018) 25:053101. doi:10.1063/1.5006613

16. Tabak M, Hammer J, Glinsky ME, Kruer WL, Wilks SC, Woodworth J, et al. Ignition and high gain with ultrapowerful lasers. *Phys Plasmas* (1994) 1:1626–34. doi:10.1063/1.870664

17. Atzeni S, Temporal M, Honrubia J. A first analysis of fast ignition of precompressed icf fuel by laser-accelerated protons. *Nucl Fusion* (2002) 42:L1–4. doi:10.1088/0029-5515/42/3/101

18. Baitin AV, Kuzanyan KM. A self-similar solution for expansion into a vacuum of a collisionless plasma bunch. *J Plasma Phys* (1998) 59:83–90. doi:10.1017/S0022377897005916

19. True MA, Albritton JR, Williams EA. Fast ion production by suprathermal electrons in laser fusion plasmas. *The Phys Fluids* (1981) 24:1885–93. doi:10.1063/1.863270

20. Mora P. Thin-foil expansion into a vacuum. *Phys Rev E* (2005) 72:056401. doi:10.1103/PhysRevE.72.056401

21. Wilks SC, Kruer WL, Tabak M, Langdon AB. Absorption of ultra-intense laser pulses. *Phys Rev Lett* (1992) 69:1383–6. doi:10.1103/PhysRevLett.69.1383

22. Kemp AJ, Divol L. Interaction physics of multipicosecond petawatt laser pulses with overdense plasma. *Phys Rev Lett* (2012) 109:195005. doi:10.1103/PhysRevLett.109.195005

23. Sorokovikova A, Arefiev AV, McGuffey C, Qiao B, Robinson APL, Wei MS, et al. Generation of superponderomotive electrons in multipicosecond interactions of kilojoule laser beams with solid-density plasmas. *Phys Rev Lett* (2016) 116:155001. doi:10.1103/PhysRevLett.116.155001

24. Iwata N, Kojima S, Sentoku Y, Hata M, Mima K. Plasma density limits for hole boring by intense laser pulses. *Nat Commun* (2018) 9:623. doi:10.1038/s41467-018-02829-5

25. Kemp AJ, Wilks SC. Direct electron acceleration in multi-kilojoule, multi-picosecond laser pulses. *Phys Plasmas* (2020) 27:103106. doi:10.1063/5.0007159

26. Iwata N, Mima K, Sentoku Y, Yogo A, Nagatomo H, Nishimura H, et al. Fast ion acceleration in a foil plasma heated by a multi-picosecond high intensity laser. *Phys Plasmas* (2017) 24:073111. doi:10.1063/1.4990703

27. Iwata N, Kemp AJ, Wilks SC, Mima K, Mariscal D, Ma T, et al. Lateral confinement of fast electrons and its impact on laser ion acceleration. *Phys Rev Res* (2021) 3:023193. doi:10.1103/PhysRevResearch.3.023193

28. Crow JE, Auer PL, Allen JE. The expansion of a plasma into a vacuum. *J Plasma Phys* (1975) 14:65–76. doi:10.1017/S0022377800025538

29. Mora P. Plasma expansion into a vacuum. *Phys Rev Lett* (2003) 90:185002. doi:10.1103/PhysRevLett.90.185002

30. Simpson RA, Mariscal DA, Kim J, Lemos N, Grace ES, Swanson KK, et al. Investigation of boosted proton energies through proton radiography of target normal sheath acceleration fields in the multi-ps regime. *Phys Plasmas* (2023) 30:103103. doi:10.1063/5.0157214

31. Iwata N, Sentoku Y, Sano T, Mima K. Plasma expansion accompanying superthermal electrons in over-picosecond relativistic laser-foil interactions. *Plasma Phys Controlled Fusion* (2019) 62:014011. doi:10.1088/1361-6587/ab4d02

32. Sentoku Y, Kemp A. Numerical methods for particle simulations at extreme densities and temperatures: weighted particles, relativistic collisions and reduced currents. *J Comput Phys* (2008) 227:6846–61. doi:10.1016/j.jcp.2008.03.043

33. Sentoku Y, Mima K, Kojima S-i., Ruhl H. Magnetic instability by the relativistic laser pulses in overdense plasmas. *Phys Plasmas* (2000) 7:689–95. doi:10.1063/1.873853

34. Kim J, Kemp AJ, Wilks SC, Kalantar DH, Kerr S, Mariscal D, et al. Computational modeling of proton acceleration with multi-picosecond and high energy, kilojoule, lasers. *Phys Plasmas* (2018) 25:083109. doi:10.1063/1.5040410